

11. Medoff BP, Brody WR, Nassi, M, Macovski A. Iterative convolution backprojection algorithms for image reconstruction from limited data. *J Opt Soc Am* 1983;73:1493-1500.
12. Walters TE, Simon W, Chesler DA, Correia JA. Attenuation correction in gamma emission computed tomography. *J Comput Assist Tomogr* 1981;5:9-94.
13. Xu XL, Liow JS, Strother SC. Iterative algebraic reconstruction algorithms for emission computed tomography: a unified framework and its application to positron emission tomography. *Med Physics* 1993;20:1675-1684.
14. Shepp LA, Vardi Y. Maximum likelihood reconstruction for emission tomography. *IEEE Trans Med Imaging* 1982;1:113-122.
15. Lange K, Carson RE. EM reconstruction algorithms for emission and transmission tomography. *J Comput Assist Tomogr* 1984;8:306-316.
16. Liow JS, Strother SC. Noise and signal decoupling in maximum likelihood reconstructions and Metz filter for PET brain images. *Phys Med Biol* 1994;39:735-750.
17. Llacer J, Andreae S, Veklerov E. Towards a practical implementation of the MLE algorithm for positron emission tomography. *IEEE Trans Nucl Sci* 1986;33:468-477.
18. Lalush DS, Tsui BMW. A fast and stable maximum a posteriori conjugate gradient reconstruction algorithm. *Med Physics* 1995;22:1273-1284.
19. Sauer K, Bouman C. A local update strategy for iterative reconstruction from projections. *IEEE Trans Signal Proc* 1993;41:534-548.
20. Fessler JA. Penalized weighted least-squares image reconstruction for positron emission tomography. *IEEE Trans Med Imaging* 1994;13:290-300.
21. Mumcuoglu E, Leahy R, Zhou Z, Cherry SR. A phantom study of the quantitative behavior of Bayesian PET reconstruction methods. *Conference Record of the 1995 IEEE Nuclear Sciences Symposium and Medical Imaging Conference*: 1995;3:1703-1707.
22. Lalush DS, Tsui BMW. Improving the convergence of iterative filtered backprojection algorithms. *Med Physics* 1993;21:1283-1286.
23. Clinthorne NH, Pan T-S, Chiao P-C, Rogers WL, Stamos JA. Preconditioning methods for improved convergence rates in iterative reconstructions. *IEEE Trans Med Imaging* 1993;12:78-83.
24. Snyder DL, Miller MI, Thomas LJ Jr, Politte DG. Noise and edge artifacts in maximum-likelihood reconstructions for emission tomography. *IEEE Trans Med Imaging* 1987;6:228-238.
25. Liow JS, Strother SC, Rottenberg DA. Improved resolution via iterative reconstruction for PET volume imaging. *Conference Record of the 1994 IEEE Nuclear Sciences Symposium and Medical Imaging Conference* 1994;3:1315-1319.
26. Palmer BM, Sajjad M, Rottenberg DA. An automated [¹⁵O]H₂O production and injection system for PET imaging. *Nucl Med Biol* 1995;22:241-249.
27. Woods RP, Mazziotta JC, Cherry SR. MRI-PET registration with automated algorithm. *J Comput Assist Tomogr* 1992;17:536-546.
28. Worsley KJ, Evans AC, Marrett S, Neelin P. A three-dimensional statistical analysis for CBF activation studies in human brain. *J Cereb Blood Flow Metab* 1992;12:900-918.
29. Liow JS, Strother SC. The convergence of object-dependent resolution in maximum likelihood based tomographic image reconstruction. *Phys Med Biol* 1993;38:55-70.
30. Schaper KA, Rehm K, Summers D, et al. Symbolic representation of functional data: the corner-cube environment. *Neuroimage* 1996;3:S166.
31. Snedecor GW, Cochran WG. *Statistical methods*. Ames, IA: Iowa State University Press; 1980.
32. Taylor SF, Minishima S, Koeppe, RA. Instability of localization of cerebral blood flow activation foci with parametric maps. *J Cereb Blood Flow Metab* 1993;13:1040-1041.
33. Worsley KJ, Evans AC, Marrett S, Neelin P. Author's reply. *J Cereb Blood Flow Metab* 1993;13:1041-1042.
34. Carson RE, Yan Y, Chodkowski B, Yap TK, Daube-Witherspoon ME. Precision and accuracy of regional radioactivity quantitation using the maximum likelihood EM reconstruction algorithm. *IEEE Trans Med Imaging* 1994;13:526-537.
35. Hudson HM, Larkin RS. Accelerated image reconstruction using ordered subsets of projection data. *IEEE Trans Med Imaging* 1994;13:601-609.

Fluorine-18-Fluoromisonidazole Radiation Dosimetry in Imaging Studies

Michael M. Graham, Lanell M. Peterson, Jeanne M. Link, Margaret L. Evans, Janet S. Rasey, Wui-Jin Koh, James H. Caldwell and Kenneth A. Krohn

Departments of Radiology and Radiation Oncology, University of Washington School of Medicine; and Division of Cardiology, Department of Medicine, Seattle Veteran's Administration Medical Center, Seattle, Washington

Fluoromisonidazole (FMISO), labeled with the positron emitter ¹⁸F, is a useful hypoxia imaging agent for PET studies, with potential applications in patients with tumors, cardiovascular disease and stroke. **Methods:** Radiation doses were calculated in patients undergoing imaging studies to help define the radiation risk of FMISO-PET imaging. Time-dependent concentrations of radioactivity were determined in blood samples and PET images of patients following intravenous injection of [¹⁸F]FMISO. Radiation absorbed doses were calculated using the procedures of the Medical Internal Radiation Dose (MIRD) committee, taking into account the variation in dose based on the distribution of activities observed in the individual patients. As part of this study we also calculated an S value for brain to eye. Effective dose equivalent was calculated using ICRP 60 weights. **Results:** Effective dose equivalent was 0.013 mSv/MBq in men and 0.014 mSv/MBq in women. Individual organ doses for women were not different from men. Assuming bladder voiding at 2- or 4-hr intervals, the critical organ that received the highest dose was the urinary bladder wall (0.021 mGy/MBq with 2-hr voiding intervals or 0.029 mGy/MBq with 4-hr voiding intervals). **Conclusion:** The organ doses for [¹⁸F]FMISO are comparable to those associated with other commonly performed nuclear medicine tests and indicate that potential radiation risks associated with this study are within generally accepted limits.

Key Words: fluorine-18-fluoromisonidazole; dosimetry; Monte Carlo simulations

J Nucl Med 1997; 38:1631-1636

Fluoromisonidazole ([¹⁸F]FMISO, [1-H-1-(3-[¹⁸F]fluoro-2-hydroxypropyl)-2-nitroimidazole], RO-07-0741) is a nitroimidazole that is structurally similar to the well-known radiosensitizer, misonidazole. Both molecules distribute throughout the total body water space, readily crossing membranes by passive diffusion. Fluorine-18-FMISO is bound and retained within viable hypoxic cells in an inverse relationship to the oxygen concentration. Binding occurs at the same range of low oxygen levels, which lead to ischemic cellular damage and increased radiation resistance (1,2). Fluorine-18-FMISO is currently being used with PET imaging to noninvasively assess hypoxia in human malignancies (3-6) and in the hearts of patients with myocardial ischemia (7). Accurate radiation dosimetry of [¹⁸F]FMISO is required to evaluate the benefits and the relative radiation-related risks. This article presents estimates of the radiation dose to various organs and to the whole body. The estimates are derived from time-activity curves of blood and normal tissue from imaging studies of patients with tumors, coronary artery disease, paralysis or arthritis.

MATERIALS AND METHODS

Patients

Biodistribution data from 60 patients (55 men, 5 women) who underwent [¹⁸F]FMISO PET scans at the University of Washington between August 1989 and January 1996 were used for dosimetry estimates. Fifty-four of the individuals had cancer and were imaged to assess tumor hypoxia before radiotherapy, three patients had histories of myocardial ischemia, two were paraplegic and one had rheumatoid arthritis. None of the patients had clinical congestive

Received Aug. 1, 1996; revision accepted Nov. 14, 1996.

For correspondence or reprints contact: Michael M. Graham, PhD, MD, Department of Radiology (Nuclear Medicine), Box 356113, University of Washington, Seattle, WA 98195.

heart failure at the time of the study. No dietary restrictions were placed on patients for study purposes, and none appeared to be clinically dehydrated during imaging. The normal tissues in the imaging data used for dosimetry were distant from the site of primary pathology. Urine samples were collected from 20 studies to calculate the dose to the bladder. The imaging procedure was approved by the institutional human subjects review committee and informed consent was obtained from all patients before imaging.

Data Collection

Patients studied before February 1994 were imaged with the UW-PET SP3000 time-of-flight PET scanner. Patients studied after February 1994 were imaged on the GE Advance PET scanner. All patients were positioned in the tomograph, and an attenuation scan was obtained with a ^{68}Ge rotating sector source. In the SP3000, following the attenuation scan, a vial containing water was replaced by a calibration vial containing a known amount of ^{18}F solution positioned beneath the imaging table within the field of view. In the GE Advance tomograph, the calibration vials were imaged separately from the patient and reconstructed using the same filter size as the emission images.

Fluorine-18-FMISO was prepared as described previously (8), and the radiopharmaceutical dose and the activity in the calibration vials were assayed in a dose calibrator before patient imaging.

Patients were injected with 3.7 MBq/kg (0.1 mCi/kg) [^{18}F]FMISO. Some of the patients were imaged continuously for 3–4 hr after injection. The majority were imaged using an abbreviated protocol (3) in which they were imaged for 1 hr beginning 2 hr after injection. Blood samples were collected during the imaging procedure and counted in a 10-detector gamma well-counter. The multiple detectors in the gamma counter were normalized with ^{68}Ge standards before use. Upon completion of the imaging study, samples of the calibration vials were also assayed in the gamma counter to cross-reference between tomograph, gamma counter and dose calibrator, thereby allowing all imaging time-activity curves to be calculated as Bq-hr per gram of tissue. All images were reconstructed with a spatial resolution of 12 mm. Performance details for each of the tomographs have been reported (9–11).

Calculation of Tissue Time-Activity Curves

The gamma counter blood and calibration vial data were background subtracted and converted from cpm/g to Bq/g using the efficiency correction factors derived from standards that were also measured in the dose calibrator. Tomograph images were reconstructed in intervals of 2–40 min. MRI and CT scans were used to align the PET attenuation corrected images to identify areas of normal tissue that were outlined as regions of interest (ROIs). Additional ROIs drawn over the calibration vials were used to determine efficiency. In the SP3000, a large ROI was drawn in the space above the body to use for background scatter correction. In the GE Advance, scatter correction was incorporated into the reconstruction algorithm. Data from each ROI for each time interval in counts/pixel were corrected for image duration and tomograph efficiency using data from the calibration vial and converted to units of Bq/g. Lung activity was corrected for tissue density ($0.36 \pm 0.12 \text{ g/cm}^3$) using the attenuation scan of a sample set of 18 patients (12). Tissue density in other organs was assumed to be 1.0 g/cm^3 . The Bq/g values were then normalized to a 1 MBq injection in a 70-kg patient. Total activity in each organ was calculated by assuming uniform distribution of activity throughout the organ and multiplying Bq/g by standard reference organ weights (13).

Since full time-activity curves were not available for individual patients imaged using the abbreviated protocol, the area under the curve (\bar{A}) needed for the MIRD calculation was obtained through

a combined patient time-activity curve for each organ. The normalized, not decay corrected, tissue activity (Bq/g) for all patients for each tissue (including blood) was plotted against time (min) and fit to the empiric function:

$$A(te^{-Bt} + C(1 - e^{-Dt})e^{-Et}) \quad \text{Eq. 1}$$

using the “Solver-Add In” function in EXCEL 4.0 (Microsoft Inc., Redmond, WA) to minimize the sum of the squares of the differences between the function and the data for each tissue. This formula was simply a gamma variate with an exponential tail used as a means to fit a curve to the combined patient data. It was not an attempt to physiologically model the kinetics of [^{18}F]FMISO. This function is more appropriate than a simple sum of exponentials since it can realistically account for the rising initial portion of the curve.

The area under the curve (\bar{A}) was obtained by adjusting the curve height (A in the empiric function) to match the individual patient data, but using the combined patient data curve shape to interpolate the rest of the time-activity curve. Thus the values of B , C , D and E were determined for each tissue from the combined patient data and not for individual patients. These values were kept fixed, and only A was adjusted to obtain an appropriate curve for each patient.

Calculation of Total Bladder Activity

The measured activity for total excreted urine for all patients was combined into one dataset and fit using the empiric formula for exponential in-growth: $A(1 - e^{-Bt})$. This was then used to estimate \bar{A} , assuming patients voided at 2- or 4-hr intervals.

Radiation Dosimetry Calculation

The distribution of absorbed dose was calculated using S values obtained from MIRDSE2 (14) according to the MIRD scheme (15). Implicit to the MIRD scheme is the assumption that the integrated activity is known for each of the source organs. Observed source organs in this study included: brain, lung, heart wall, blood (heart chamber), marrow, liver, kidney, gastrointestinal tract (accounting for activity in the small intestine, upper and lower large intestine) and bladder. Bladder integrated activity was calculated assuming repetitive voiding at either 2- or 4-hr intervals, as described above. Source organ uptake varied between individuals, implying there was also a range of absorbed doses associated with the target organs. We estimated the range of absorbed doses to the target organs by using Monte Carlo simulation, repeating the following three steps 1000 times: (a) The integrated activity for each measured tissue was randomly chosen from the source organ data; (b) the dose to unobserved organs was calculated by assuming that all unaccounted activity was uniformly distributed throughout the body; and (c) the radiation doses to all target organs were calculated using S values according to the MIRD scheme. This scheme generated a distribution of expected radiation doses to the target organs. The process was done using a spreadsheet program (EXCEL 4.0 by Microsoft Inc., Redmond, WA) and a Monte Carlo program (Crystal Ball 3.0 by Decisioneering Inc., Denver, CO).

Since there is no reported S value for the dose from the brain to the lens of the eye, it was calculated, assuming the lens was located 2 cm from the surface of the brain and by integrating the contributions from the brain in 1 cm increments. This calculation assumes uniform distribution of activity in the brain, which should be reasonable for the lipophilic [^{18}F]FMISO. The S value for the lens by this approach was $1.2 \times 10^{-5} \text{ Gy/MBq-hr}$ ($4.3 \times 10^{-5} \text{ rads}/\mu\text{Ci-hr}$). Images of the head showed no excessive accumulation of activity in the area of the eye. The dose to the lens was calculated using the above S value for brain; the S values for thyroid as the target organ were used for all other sources. This approach should yield a slight overestimate of the radiation dose to

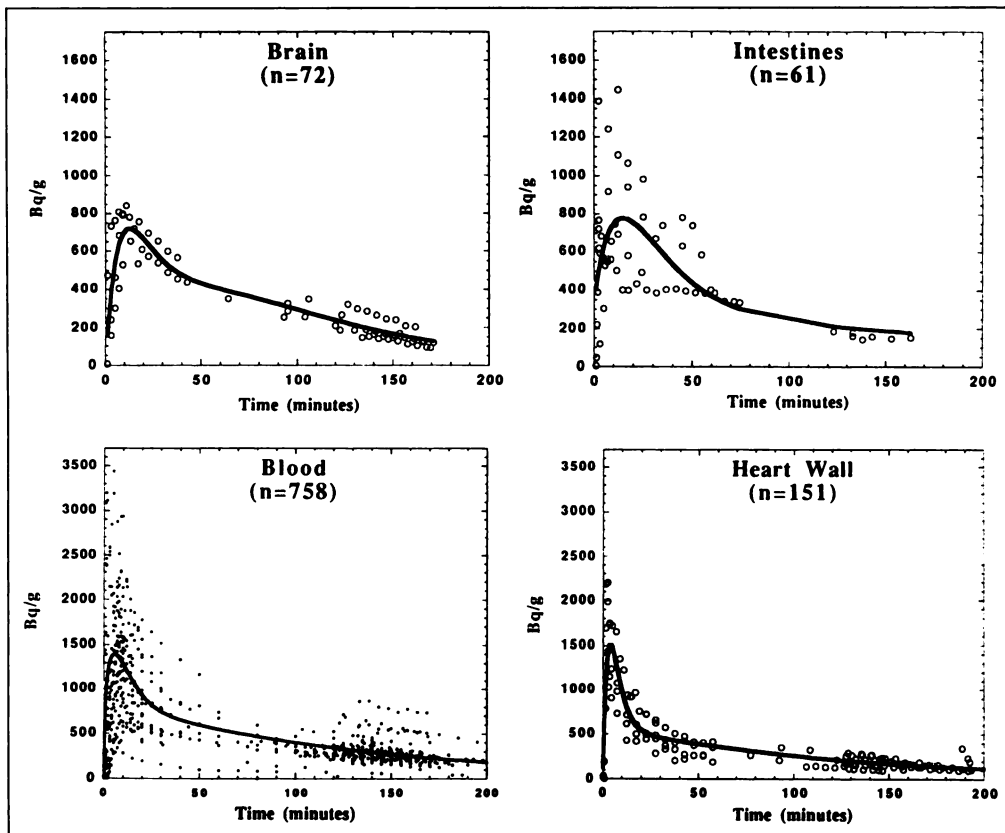


FIGURE 1. Activity of $[^{18}\text{F}]$ FMISO in the source organs: brain, intestines, blood (heart chamber) and heart wall with the best fit curve used to determine \bar{A} for individual patients. The data has been normalized to 1 MBq injected per 70 kg body weight.

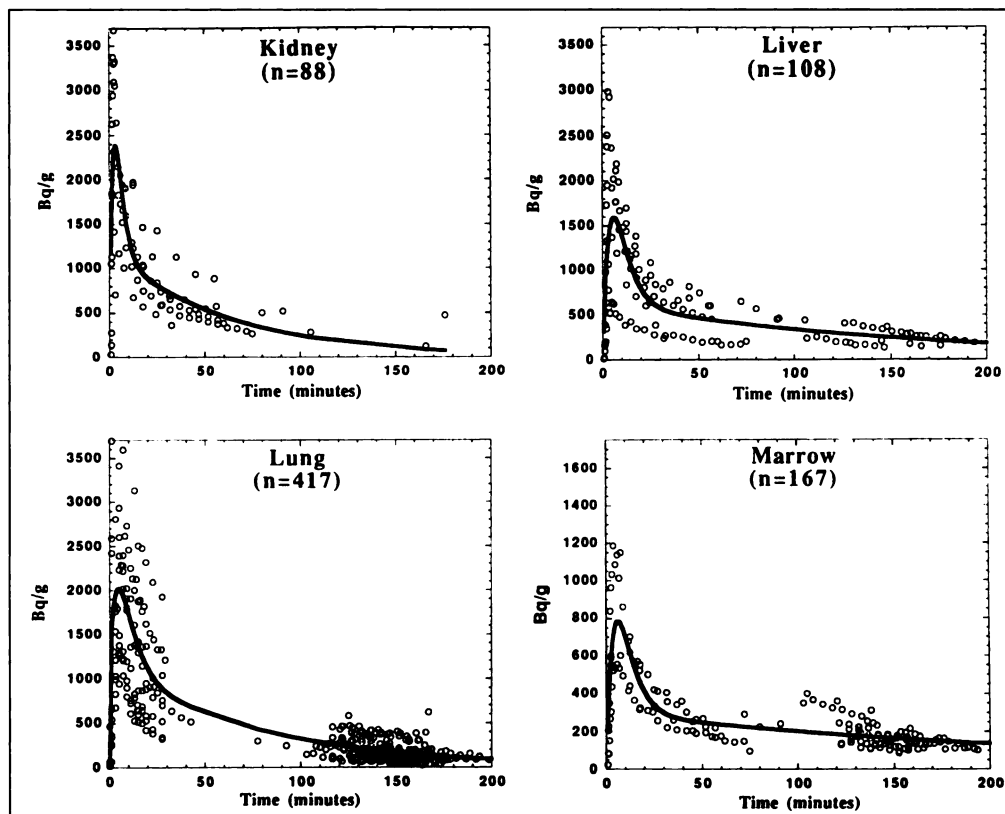


FIGURE 2. Activity of $[^{18}\text{F}]$ FMISO in the source organs: kidney, liver, lung and marrow with the best fit curve used to determine \bar{A} for individual patients. The data has been normalized to 1 MBq injected per 70 kg body weight.

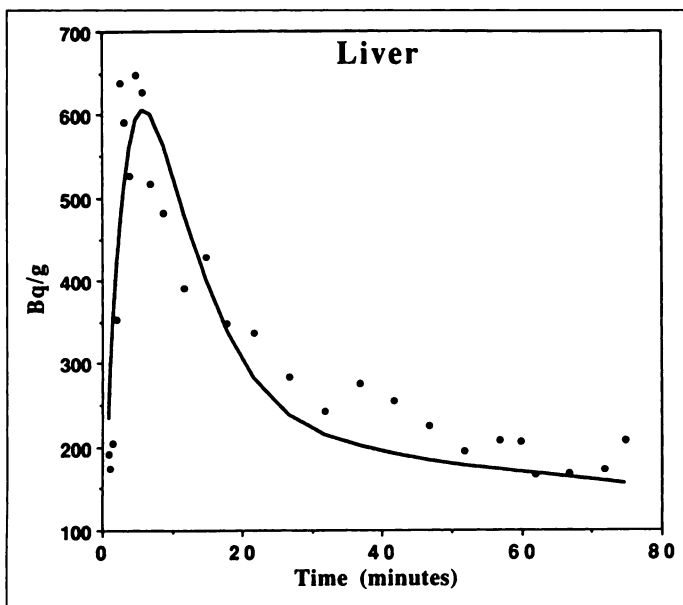


FIGURE 3. Activity of $[^{18}\text{F}]$ FMISO in a liver curve with the best fit curve used to determine \bar{A} . The best fit curve was determined by fitting function (1) to all the liver data. Only the scaling term, A , was varied to fit the curve to this dataset. The data has been normalized to 1 MBq injected per 70 kg body weight.

the lens since the thyroid is somewhat closer to most of the source organs than the eye.

Effective dose equivalent to uniform whole-body exposure was calculated using the weights published in ICRP 60 (16), assuming a relative biological effectiveness of 1.0. The dose estimates for the gonads, bone marrow, colon, lung, stomach, bladder, breasts, liver, esophagus (assumed to be the same as stomach), thyroid, skin, bone surface and remainder of body were multiplied by their appropriate weights and summed to calculate effective dose equivalents for men and women.

RESULTS

All the data were normalized for a 1-MBq injection into a 70-kg man. The clearance curves for the combined patient data for each of the source organs determined are shown in Figures 1 and 2. Figure 3 illustrates a sample liver curve that has been fit, by simple scaling, with the best fit curve from the entire set of liver data. Blood clearance is characterized by a rapid distribution phase, followed by a first order elimination phase. Most organs equilibrate with blood FMISO levels within minutes of injection. The mean area under the curve (\bar{A}) and s.d. for each

TABLE 1
Tissue Uptake of Fluorine-18-FMISO for an Injection of 37 MBq

Organ	Wt* (g)	\bar{A} (MBq hr)		n† (ROI)
		mean	s.d.	
Brain	1420	1.5	0.3	10 (72)
Intestines	798	1.8	0.8	7 (61)
Heart chamber (blood)	454	0.85	0.4	55 (766)
Heart wall	316	0.42	0.09	13 (151)
Kidneys	299	0.46	0.15	12 (88)
Liver	1910	4.0	1.8	12 (108)
Lungs	1000	2.0	1.1	35 (417)
Marrow	1120	1.1	0.4	17 (167)

*Weights are from (13) for a 70 kg adult male.

†n (number of patients) is followed by the number of ROIs (in parentheses).

observed source organ, along with the number of patients and ROIs, are shown in Table 1.

Accumulation of activity in the bladder is presented as voided urine activity and the curve fit for exponential in-growth in Figure 4. The mean calculated integral activity, with voiding at 2 hr intervals, was 24.5 kBq/hr, and with 4-hr voiding intervals was 41.9 kBq/hr.

The median dose and the 25th and 75th percentiles, as determined from the Monte Carlo simulations, assuming bladder voiding every 2 hr, for each organ are presented in Table 2. Bladder voiding every 4 hr resulted in an increased dose to the bladder, but not to other organs, so only the 2-hr voiding doses are shown. The highest radiation absorbed dose was to the bladder wall (0.021 mGy/MBq or 0.029 mGy/MBq, respectively, with 2 or 4 hr voiding intervals). The calculated total-body dose for a 70-kg man injected with $[^{18}\text{F}]$ FMISO was 0.013 mGy/MBq. The calculated total-body dose for a 57-kg woman was 0.016 mGy/MBq. Since the absorbed doses to individual organs for females were virtually the same as the male organs, the data were combined and reported here using the S tables for the adult male. The effective dose equivalent (ICRP 60) was calculated to be 0.013 mSv/MBq for men and 0.014 mSv/MBq for women (16).

DISCUSSION

Fluoromisonidazole shows substantial promise as a hypoxia imaging agent. PET imaging of $[^{18}\text{F}]$ FMISO in patients with tumors indicates that this test can quantify hypoxia. When fully validated, this procedure may be used to guide appropriate, physiologically based treatment for patients with medical conditions in which hypoxia influences response to therapy. The nanomolar dose of $[^{18}\text{F}]$ FMISO used in these tracer studies is approximately one ten-thousandth of the dose of misonidazole used clinically. No chemotoxicity from $[^{18}\text{F}]$ FMISO was expected nor has any been noted (17). This present investigation therefore concerns only the radiation exposure issues to better define the radiation risk of $[^{18}\text{F}]$ FMISO PET imaging.

In addition to the simplifications inherent in the MIRD phantom model (14,15), additional assumptions were made in analysis of our data. The most important assumptions were as follows:

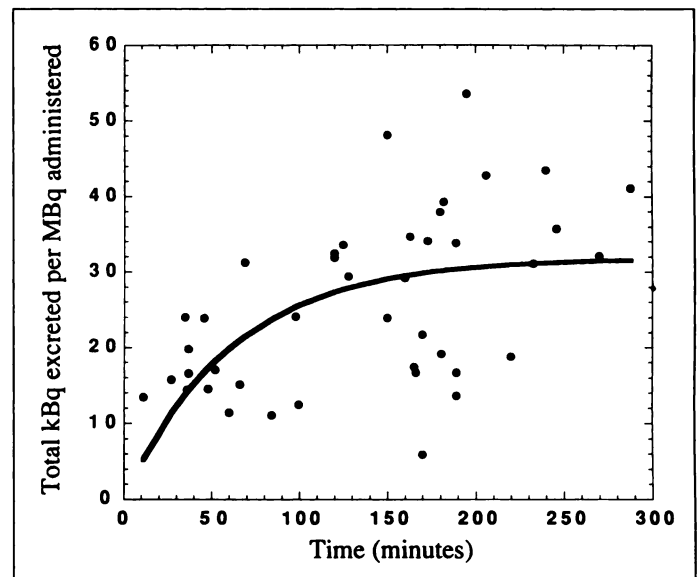


FIGURE 4. Integrated $[^{18}\text{F}]$ FMISO urine activity of 42 samples from 20 studies normalized to 1 MBq injection per 70 kg body weight. The line is the best fit curve used to determine \bar{A} for individual patients. Note that the mean total excretion is about 30 kBq, or 3% of the injected dose.

TABLE 2
Radiation Absorbed Dose to Organs

Target organ	2 hr voids (median mGy/MBq)	Percentiles (mGy/MBq)	
		25%	75%
Adrenals	0.0166	0.0165	0.0167
Brain	0.0086	0.0080	0.0093
Breasts	0.0123	0.0122	0.0124
Gall bladder wall	0.0148	0.0145	0.0150
Lower large intestine	0.0143	0.0121	0.0152
Small intestine	0.0132	0.0109	0.0142
Stomach	0.0126	0.0126	0.0127
Upper large intestine	0.0140	0.0113	0.0150
Heart wall	0.0185	0.0171	0.0199
Kidney	0.0157	0.0143	0.0180
Liver	0.0183	0.0163	0.0206
Lungs	0.0099	0.0092	0.0114
Muscle	0.0142	0.0141	0.0143
Ovaries	0.0176	0.0174	0.0178
Pancreas	0.0179	0.0178	0.0179
Red marrow	0.0109	0.0103	0.0116
Bone surface	0.0077	0.0076	0.0079
Skin	0.0048	0.0048	0.0048
Spleen	0.0163	0.0163	0.0165
Testes	0.0146	0.0145	0.0148
Thymus	0.0155	0.0153	0.0156
Thyroid	0.0151	0.0150	0.0152
Urinary bladder wall	0.0210	0.0164	0.0239
Uterus	0.0183	0.0181	0.0186
Eye lens	0.0154	0.0153	0.0155
Total body	0.0126	0.0126	0.0126

1. Tracer distribution was assumed to be homogeneous throughout each organ.
2. Tracer clearance was through both biological and physical decay during the course of an imaging study, but clearance was assumed to occur by only physical decay after the final imaging time point. This was a conservative assumption that would lead to overestimation of the actual radiation exposure.
3. Accumulated bladder activity was calculated based on repeated voiding every 2 or 4 hr.
4. Since full tissue curves for each patient were unavailable, a scaled best fit curve shape was used to calculate \bar{A} for individual patients.

Our results were checked for plausibility by a simple calculation. Assuming that 100% of the injected dose (1 MBq) was evenly distributed and retained throughout the body, the \bar{A} for the total body should be:

$$1 \text{ MBq} \int_0^{\infty} e^{-\frac{0.693}{1.83} t} dt = 2.641 \text{ MBq} \cdot \text{hr.} \quad \text{Eq. 2}$$

Since the S value for total body \rightarrow total body in 70-kg men is $4.9 \times 10^{-6} \text{ Gy/MBq} \cdot \text{hr}$ ($1.8 \times 10^{-5} \text{ rads}/\mu\text{Ci}\cdot\text{hr}$), the whole-body dose should be 0.013 mGy/MBq or 48 mrad/mCi. For 57-kg women, the S value for total body \rightarrow total body is $5.9 \times 10^{-6} \text{ Gy/MBq}\cdot\text{hr}$ ($2.2 \times 10^{-5} \text{ rads}/\mu\text{Ci}\cdot\text{hr}$) making the whole-body dose 0.016 mGy/MBq, or 58 mrad/mCi. These conservative, average whole-body doses are within the range of doses calculated for individual organs (0.0048–0.029 mGy/MBq) and agree well with the calculated whole-body dose of

0.013 mGy/MBq (Table 2). The two approaches yield essentially the same numbers because [^{18}F]FMISO is lipophilic and distributes relatively evenly throughout the body. Only a small amount is lost through the kidneys (3%–4% during the entire study), so most of the activity remains in the body until it decays. These values are also consistent with the effective dose equivalent calculation of 0.0134 mSv/MBq and 0.0140 mSv/MBq for men and women, respectively.

The octanol:water partition coefficient of FMISO is 0.40 (18), implying that it is freely diffusible throughout most tissues. Time-activity curves show that FMISO concentrations in tissues such as brain and muscle equilibrate with blood within 10–20 min of injection. Increased retention in other normal tissues can be attributed to specific physiologic processes. Metabolism of nitroimidazoles occurs in the liver (19), and excretion occurs principally through the kidneys and bladder (20), resulting in increased radiation dose to these organs.

The PET acquisition of [^{18}F]FMISO tissue time-activity curves provides data for the calculation of cumulative radiation doses to each organ that is accurate only within the counting limitations and spatial resolution of the tomograph. Thus, dosimetry calculations of small organs which can not be visualized, such as the adrenals, ovaries or testes, were done assuming average total-body concentrations in those sites. Images that included these organs did not suggest any remarkable accumulation of activity.

There is substantial noise in some of the data presented, particularly in Figure 4, the total activity excreted in urine. This variation presumably arises from a wide variation in degree of hydration and renal function in these patients. The variation in the activity plots for other tissues is to some extent due to the relatively large numbers of patients imaged between 100 and 200 min. The curves from individual patients did not increase during that time. An example of a typical tissue imaged continuously is shown in Figure 3.

The relatively wide range of activities seen in the various organs implies a relatively wide range of absorbed radiation doses. A Monte Carlo simulation method was used to estimate this range. The Monte Carlo method was used to randomly select the measured activity in different source organs and then calculate the absorbed doses to the various other target organs. This process was repeated 1000 times to obtain a distribution of absorbed doses. The main reason this approach was used was to estimate the variation in radiation doses that might be expected from individual to individual. An interesting effect that was seen in doing the Monte Carlo simulation was that the variation in estimated doses to target organs was less than the variation of activity in the source organs. This is because a large fraction of the absorbed doses to the target organs arises from the activity distributed in the “remainder of body.” The activity in the “remainder of body” is relatively constant since it is due to the activity injected minus the activity in all the measured source organs and minus the activity lost in the urine. Overall, the Monte Carlo method shows that the estimated radiation doses do not vary markedly between organs or between individual subjects, in spite of the wide variation in the data shown in Figures 1 and 2. In actual practice the main factor that will result in variation in dose will be patient weight. The average absorbed dose will be directly related to the administered dose per kilogram of body weight.

CONCLUSION

To adequately assess a benefit-to-risk ratio, the potential benefits of a procedure must be well defined. The organ and

total-body doses associated with [¹⁸F]FMISO PET imaging are comparable to or lower than those associated with other widely used clinical nuclear medicine procedures (21–24). The radiation exposure to the critical organ, the bladder wall, could be reduced slightly by increased frequency of bladder voiding.

Ongoing clinical trials using [¹⁸F]FMISO-PET imaging will establish its appropriate role in the diagnosis and management of patients with tumors, ischemic heart disease and stroke, thereby defining the benefit. Should [¹⁸F]FMISO-PET imaging be validated as a useful clinical test, this analysis indicates that the radiation absorbed dose resulting from the imaging procedure is favorable for further use of this imaging agent.

ACKNOWLEDGMENT

We thank Gary Martin for the use of his patients' images; Barbara Lewellen, Nancy Bardou, Lay Chin and Bart Staker for assistance in the studies and collection of data; John Grierson and Aaron Charlop for providing the [¹⁸F]FMISO; Finbarr O'Sullivan for the statistics advice; and Thomas Lewellen for technical assistance in operating the tomographs. This work was supported by NIH grants CA42045, HL38736 and HL50239.

REFERENCES

1. Rasey JS, Grunbaum Z, Magee S, et al. Characterization of radiolabeled fluoromisonidazole as a probe for hypoxic cells. *Radiat Res* 1987;111:292–304.
2. Martin GV, Cerqueira MD, Caldwell JH, Rasey JS, Embree L, Krohn KA. Fluoromisonidazole: a metabolic marker of myocyte hypoxia. *Circ Res* 1990;67:240–244.
3. Koh W-J, Rasey JS, Evans ML, et al. Imaging of hypoxia in human tumors with [¹⁸F]fluoromisonidazole. *Int J Radiat Oncol Biol Phys* 1992;22:199–212.
4. Koh WJ, Bergman KS, Rasey JS, et al. Evaluation of oxygenation status during fractionated radiotherapy in human nonsmall cell lung cancers using [¹⁸F]fluoromisonidazole PET. *Int J Radiat Oncol Biol Phys* 1995;33:391–398.
5. Rasey JS, Koh W-J, Evans ML, et al. Quantifying regional hypoxia in human tumors with positron emission tomography of [¹⁸F]fluoromisonidazole: a pre-therapy study of 37 patients. *Int J Radiat Oncol Biol Phys* 1996;36:417–425.
6. Valk PE, Mathis CA, Prados MD, Gilbert JC, Budinger TF. Hypoxia in human gliomas: demonstration by PET with fluorine-18-fluoromisonidazole. *J Nucl Med* 1992;33:2133–2137.

7. Revenaugh JR, Caldwell JH, Martin GV, Grierson JL, Krohn KA. PET imaging of myocardial hypoxia with ¹⁸F-fluoromisonidazole in postmyocardial infarction patients [Abstract]. *Circulation* 1991;84(suppl 1):424.
8. Grierson JR, Link JM, Mathis CA, Rasey JS, Krohn KA. A radiosynthesis of fluorine-18-fluoromisonidazole. *J Nucl Med* 1989;30:343–350.
9. Lewellen TK, Bice AN, Harrison RL, Pencke MD, Link JM. Performance measurements of the SP3000/UW time-of-flight emission tomograph. *IEEE Trans Nucl Sci* 1988;35:665–667.
10. Lewellen TK, Kohlmyer SG, Miyaoka RS, Schubert SF, Stearns CW. Investigation of the count rate performance of the General Electric Advance positron emission tomograph. *IEEE Trans Nucl Sci* 1995;42:1051–1057.
11. DeGrado T, Turkington T, Williams J, Stearns C, Hoffman J. Performance characteristics of a whole-body PET scanner. *J Nucl Med* 1994;35:1398–1406.
12. Rhodes CG, Wollmer P, Fazio F, Jones T. Quantitative measurement of regional extravascular lung density using positron emission and transmission tomography. *J Comput Assist Tomogr* 1981;5:783–791.
13. Masses of source regions in the Cristy and Eckerman phantom series. Table III. Radiopharmaceutical Internal Dose Center, Oak Ridge Associated Universities. Oak Ridge, TN; 1986.
14. MIRDOSE2. Radiopharmaceutical Internal Dose Center, Oak Ridge Associated Universities. Oak Ridge, TN; 1986.
15. Snyder WS, Ford MR, Warner GG, Watson SB. "S" absorbed dose per unit cumulated activity for selected radionuclides and organs. *Medical Internal Radiation Dose Committee (MIRD) Pamphlet No. 11*. New York: Society of Nuclear Medicine; 1975.
16. ICRP, 1990. Recommendations of the international commission on radiological protection. ICRP Publication 60. Pergamon Press, Oxford; 1990.
17. Koh W-J, Rasey JS, Evans ML, et al. Fractional hypoxic volume and reoxygenation in human tumors [Abstract]. *Radiother Oncol* 1992;24(suppl):S112.
18. Grunbaum Z, Freauff SJ, Krohn KA, Wilbur DS, Magee S, Rasey JS. Synthesis and characterization of congeners of misonidazole for imaging hypoxia. *J Nucl Med* 1987;28:68–75.
19. Josephy PD, Mason RP. Nitroimidazoles. In: Anders MW, ed. *Bioactivation of foreign compounds*. New York: Academic Press; 1985:451–483.
20. Flockhart IR, Large P, Troup D, Malcolm SL, Marten TR. Pharmacokinetic and metabolic studies of the hypoxic cell radiosensitizer misonidazole. *Xenobiotica* 1978;8:97–105.
21. Mejia AA, Nakamura T, Masotoshi I, Hatazawa J, Masaki M, Watanuki S. Estimation of absorbed doses in humans due to intravenous administration of fluorine-18-fluorodeoxyglucose in PET studies. *J Nucl Med* 1991;32:699–706.
22. Graham LS, Krishnamurthy GT, Blahd BT. Dosimetry of skeletal-seeking radiopharmaceuticals [Abstract]. *J Nucl Med* 1974;15:496.
23. MIRD Dose Estimate Report No 10. Radiation absorbed dose from albumin microspheres labeled with ^{99m}Tc. *J Nucl Med* 1982;23:915–917.
24. Wackers FJT, Berman DS, Maddahi J, et al. Technetium-99m hexakis 2-methoxyisobutyl isonitrile: human biodistribution, dosimetry, safety and preliminary comparison to thallium-201 for myocardial perfusion imaging. *J Nucl Med* 1989;30:301–311.

Demonstration of Rectosigmoid Fistula Dynamic Scintigraphic Peritoneography

Hussein M. Abdel-Dayem, Stephane Lubicz and Arthur Radin

Nuclear Medicine Section and Section of Medical Oncology, Departments of Nuclear Medicine, Obstetrics and Gynecology and Medicine, New York Medical College, Valhalla, and St. Vincent's Hospital and Medical Center, New York, New York

Intraperitoneal installation of chemotherapy through a Mediport implanted subcutaneously in the abdominal wall is used currently for treatment of peritoneal metastases from ovarian, gastric and colonic carcinoma. There is a variable incidence of complications due to the procedure reported in the literature. The main predisposing factor for these complications is the inhomogeneous distribution of the chemotherapeutic drugs within the peritoneal cavity. We report an unusual case of a rectosigmoid fistula that developed 6 wk following the insertion of a Bardport subcutaneously in the abdominal wall for intraperitoneal therapy. The fistula was clearly demonstrated by dynamic scintigraphic peritoneography. This is a new modification of scintigraphic peritoneography as practiced routinely. We endorse the previous recommendation that scintigraphic peritoneography be

performed before every intraperitoneal installation of a chemotherapeutic drug or radiopharmaceutical to ensure the homogeneous distribution of the drugs and to prevent complications.

Key Words: intraperitoneal chemotherapy; peritoneography; ovarian cancer; colon cancer; gastric cancer

J Nucl Med 1997; 38:1636–1639

Intraperitoneal instillation of cisplatin, interferon or ³²P chromic phosphate, alone or in combination with intravenous chemotherapy, has been reported as an acceptable approach for the treatment of peritoneal carcinomatosis in patients with ovarian, colonic or gastric carcinoma (1–9). To facilitate the frequent intraperitoneal installation of the chemotherapeutic drugs or radiolabeled phosphate, special catheters (modified Tenckhoff), needles (veress) or peritoneal ports have been

Received Oct. 9, 1996; accepted Dec. 5, 1996.

For correspondence or reprints contact: Hussein M. Abdel-Dayem, MD, St. Vincent's Hospital and Medical Center, Nuclear Medicine Service, 153 West 11th St., New York, NY 10011.